

Estimating near-wall diffusion coefficients of arbitrarily shaped rigid macromoleculesMaciej Długosz ^{*}*Institute of Experimental Physics, Faculty of Physics, University of Warsaw, 02-093 Warsaw, Pasteura 5, Poland*Bogdan Cichocki  and Piotr Szymczak *Institute of Theoretical Physics, Faculty of Physics, University of Warsaw, 02-093 Warsaw, Pasteura 5, Poland*

(Received 15 February 2022; accepted 10 July 2022; published 29 July 2022)

We developed a computationally efficient approach to approximate near-wall diffusion coefficients of arbitrarily shaped rigid macromolecules. The proposed method relies on extremum principles for Stokes flows produced by the motion of rigid bodies. In the presence of the wall, the rate of energy dissipation is decreased relative to the unbounded fluid. In our approach, the position- and orientation-dependent mobility matrix of a body suspended near a no-slip plane is calculated numerically using a coarse-grained molecular model and the Rotne-Prager-Yamakawa description of hydrodynamics. Effects of the boundary are accounted for via Blake's image construction. The matrix components are scaled using ratios of the corresponding bulk values evaluated for the detailed representation of the molecule and its coarse-grained model, leading to accurate values of the near-wall diffusion coefficients. We assess the performance of the approach for two biomolecules at different levels of coarse-graining.

DOI: [10.1103/PhysRevE.106.014407](https://doi.org/10.1103/PhysRevE.106.014407)**I. INTRODUCTION**

Diffusion of macromolecules near confining surfaces is of fundamental importance in many research areas including physics and biophysics, chemistry, and nanotechnology [1–14]. Hydrodynamic interactions with boundaries introduce an additional, anisotropic drag acting on molecules [15–18]. Consequently, diffusion coefficients of arbitrarily shaped bodies become complicated functions of their position and orientation relative to boundaries [15,16,19–27]. Although analytic (and usually somewhat approximate) forms of mobility functions are available for cases such as an isotropic [15,16,28] or an axisymmetric [23] object suspended near a planar wall, more complicated shapes and boundary conditions require the application of numerical approaches: the boundary integral [29], finite element [24], and fluctuating hydrodynamics [30,31] methods, mesoscopic molecular dynamics [32], or methods in which complex shapes of molecules are composed of rigidly connected spherical components [33,34]. These are often costly in terms of computing resources. Cost can be lowered by coarse-graining representations of molecules. Simplified models neglect details of molecular shapes to benefit from simplicity and computational efficiency. Inevitably, they also introduce errors in calculated mobility functions.

We developed an approach that results in accurate approximations to the near-wall diffusion coefficients of arbitrarily shaped molecules, while using coarse-grained representations of their shapes. Our method is based on the work of Hill and Power [35]. These authors proved a pair of complementary

extremum principles, which define upper and lower bounds on the total energy dissipation rate for the Stokes flow produced by the motion of a rigid body. They showed how these can be used to obtain the drag on a body translated and rotated in a fluid. Moreover, we draw from the results presented by Kim and Karilla [36], who applied the theorems established by Hill and Power, to energy dissipation in mobility problems. In our method, a low-resolution, coarse-grained model of the molecule, consisting of only a few spherical subunits, is placed near a no-slip plane, in a given position and orientation. The mobility matrix is calculated using the Rotne-Prager-Yamakawa tensor [37,38] and Blake's image construction [39]. Accurate values of mobilities are obtained by appropriately scaling matrix components. We derive scaling factors from the components of the bulk mobility matrix obtained for a detailed model of the molecule (in our case, its shell model [34,40–42]) and the components of the bulk mobility matrix obtained for its coarse-grained model. Only a single calculation of bulk mobilities is required as the resulting scaling factors can be used to obtain near-wall mobilities for any position and orientation of the molecule relative to the wall.

The remainder of the paper is structured as follows. We begin by presenting some concepts regarding evaluation of the near-wall mobility matrix of an arbitrarily shaped body, modelled as a conglomerate of spheres. Then we introduce and justify, using energy dissipation arguments, the scaling approach to approximate near-wall mobilities. Finally, we illustrate the performance of the method for two biomolecules: a typical globular protein hen egg-white lysozyme (HEWL, Fig. 1) and a 20 bp B-DNA duplex (DNA, Fig. 2), and evaluate its range of validity.

^{*}Maciej.Dlugosz@fuw.edu.pl

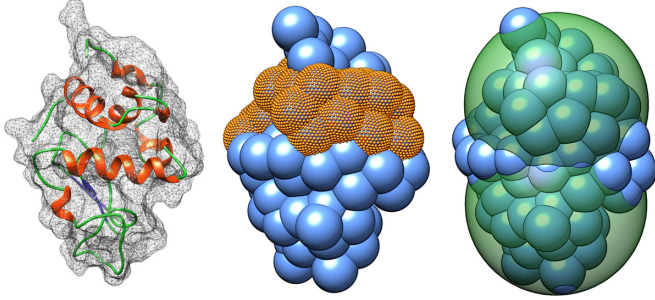


FIG. 1. Left: hen egg-white lysozyme (cartoon representation, PDB ID 6LYZ [60]) and its van der Waals surface (mesh). Center: one-bead-per-residue (medium size spheres) and shell (small spheres) models of HEWL. Right: coarse-grained dumbbell model of HEWL (large spheres). The drawings were done using the UCSF Chimera package [61].

II. HYDRODYNAMIC INTERACTIONS

The following relation holds for a rigid body of an arbitrary shape, suspended in an incompressible fluid, provided that the Reynolds number is low and the creeping flow equations [43,44] are applicable:

$$\begin{pmatrix} \mathbf{V} \\ \mathbf{\Omega} \end{pmatrix} = \begin{pmatrix} \boldsymbol{\mu}^{tt} & \boldsymbol{\mu}^{tr} \\ \boldsymbol{\mu}^{rt} & \boldsymbol{\mu}^{rr} \end{pmatrix} \cdot \begin{pmatrix} \mathbf{F} \\ \mathbf{T} \end{pmatrix}, \quad (1)$$

where \mathbf{V} and $\mathbf{\Omega}$ denote, respectively, translational and rotational velocities, \mathbf{F} and \mathbf{T} are the forces and torques that act on the body, and the 6×6 matrix represents the mobility

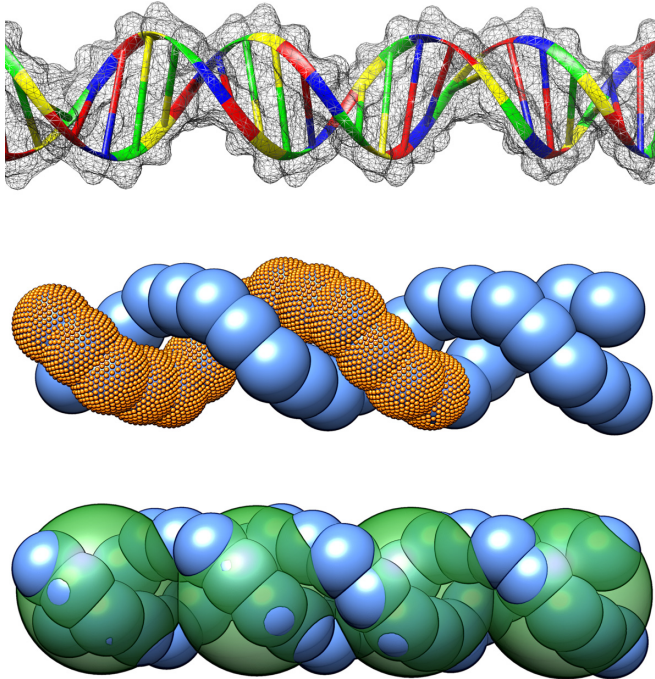


FIG. 2. Top: 20 bp DNA B-helix (cartoon representation) and its van der Waals surface (mesh). Center: one-bead-per-residue (medium-size spheres) and shell (small spheres) models of DNA. Bottom: coarse-grained four-sphere DNA model (large spheres). The drawings were made using the UCSF Chimera package [61].

tensor [44] of the body, $\boldsymbol{\mu}$. Its four blocks correspond to the body translations (tt) and rotations (rr), and their couplings (tr and rt , with $\boldsymbol{\mu}^{rt}$ being the transpose of $\boldsymbol{\mu}^{tr}$). Assuming that the system is at thermodynamic equilibrium, the fluctuation-dissipation theorem [45] relates the mobility tensor and the diffusion tensor, \mathbf{D} (k_B is the Boltzmann constant and T is the temperature):

$$\mathbf{D} = \begin{pmatrix} \mathbf{D}^{tt} & \mathbf{D}^{tr} \\ \mathbf{D}^{rt} & \mathbf{D}^{rr} \end{pmatrix} = k_B T \begin{pmatrix} \boldsymbol{\mu}^{tt} & \boldsymbol{\mu}^{tr} \\ \boldsymbol{\mu}^{rt} & \boldsymbol{\mu}^{rr} \end{pmatrix} = k_B T \boldsymbol{\mu}. \quad (2)$$

Usabiaga *et al.* [33] described a technique and provided codes (*RigidMultiBlobsWall* package) for numerically solving the mobility problem for suspensions of rigid bodies of complex shapes in Stokes flow, in unconfined, partially confined, and fully confined geometries. What follows is the basic concept of mobility calculations for the general case of a macromolecule of an arbitrary shape suspended either in an unbounded solvent or near a no-slip planar boundary.

Similarly to the previous approaches [34,40,41,46–51], the authors of Ref. [33] construct the molecules as rigid conglomerates of spherical subunits. For N such subunits of hydrodynamic radius a , suspended in an unbounded medium, the authors evaluate the hydrodynamic interactions using the $3N \times 3N$ Rotne-Prager-Yamakawa (RPY) translational mobility tensor, \mathcal{M} [37,38], the 3×3 blocks of which are given by

$$\mathcal{M}_{ii} = \frac{1}{6\pi\eta a} \mathbf{I}, \quad (3)$$

and for $i \neq j$,

$$\begin{aligned} \mathcal{M}_{ij} &= \begin{cases} \frac{1}{6\pi\eta a} \left[\left(\frac{3a}{4r_{ij}} + \frac{a^3}{2r_{ij}^3} \right) \mathbf{I} + \left(\frac{3a}{4r_{ij}} - \frac{3a^3}{2r_{ij}^3} \right) \frac{r_{ij} \otimes r_{ij}}{r_{ij}^2} \right] & r_{ij} > 2a, \\ \frac{1}{6\pi\eta a} \left[\left(1 - \frac{9r_{ij}}{32a} \right) \mathbf{I} + \left(\frac{3r_{ij}}{32a} \right) \frac{r_{ij} \otimes r_{ij}}{r_{ij}^2} \right] & r_{ij} \leq 2a. \end{cases} \end{aligned} \quad (4)$$

In the above equations, indices i and j run over spheres, η is the viscosity of the surrounding medium, r_{ij} is the distance vector between spheres i and j , \mathbf{I} is the 3×3 identity matrix, and \otimes denotes the dyadic product. In the presence of a single no-slip boundary, analytic corrections derived in Ref. [52] based on Blake image construction [39] are added to \mathcal{M}_{ii} and \mathcal{M}_{ij} . These corrections account for contributions to the mobility tensor due to the hydrodynamic interactions of the spheres with the wall. For example, corrected self mobilities of the i th sphere, in directions parallel (\parallel) and perpendicular (\perp) to the no-slip planar boundary, are given with the following functions of the sphere-wall distance, h [52]:

$$\mathcal{M}_{ii,\parallel}(h) = \frac{1}{6\pi\eta a} \left(1 - \frac{9a}{16h} + \frac{a^3}{8h^3} - \frac{a^5}{16h^5} \right), \quad (5)$$

$$\mathcal{M}_{ii,\perp}(h) = \frac{1}{6\pi\eta a} \left(1 - \frac{9a}{8h} + \frac{a^3}{2h^3} - \frac{a^5}{8h^5} \right). \quad (6)$$

The reader may compare these functions to an exact analytical solution derived by Brenner [16] [Eq. (A1)] and approximations proposed by DeLong *et al.* [53] [Eqs. (A2) and (A3)]. Due to the axial symmetry of the sphere with its image system, all but the diagonal elements of the sphere self mobility matrix

vanish. The expression for the correction to \mathcal{M}_{ij} is quite lengthy, and we choose not to present it here. It can be found in either Ref. [52] or Ref. [54].

The spherical subunits that make up the rigid body are constrained to move rigidly according to the following condition [33]:

$$\mathbf{v}_i = \mathbf{V} + \boldsymbol{\Omega} \times (\mathbf{r}_i - \mathbf{r}), \quad (7)$$

where the index i runs over the subunits, \mathbf{v}_i is the velocity of the i th subunit, $\mathbf{r}_i = (x_i, y_i, z_i)$ is the position of the i th subunit, $\mathbf{r}(x, y, z)$ is the position of the chosen reference point within the rigid body. In the current work the reference point is chosen to be the mobility center of the rigid body [44,55–57], in which the long-time translational self-diffusion coefficient is uniquely determined by the trace of the translational-translational block of the mobility matrix [56,57], and in which the rt block of the mobility matrix, $\boldsymbol{\mu}$, is symmetric. Its position can be found once all components of $\boldsymbol{\mu}$ in any coordinate system are known [44,55].

The above equation can be written as

$$\begin{pmatrix} \mathbf{v}_1 \\ \vdots \\ \mathbf{v}_N \end{pmatrix} = \mathcal{K} \cdot \begin{pmatrix} \mathbf{V} \\ \boldsymbol{\Omega} \end{pmatrix}, \quad (8)$$

where the $3N \times 6$ matrix \mathcal{K} is defined as

$$\mathcal{K} = \begin{pmatrix} \mathbf{I} & (\mathbf{r} - \mathbf{r}_1) \times \\ \dots & \dots \\ \mathbf{I} & (\mathbf{r} - \mathbf{r}_N) \times \end{pmatrix}, \quad (9)$$

with

$$(\mathbf{r} - \mathbf{r}_i) \times = \begin{pmatrix} 0 & -(z - z_i) & y - y_i \\ z - z_i & 0 & -(x - x_i) \\ -(y - y_i) & x - x_i & 0 \end{pmatrix}. \quad (10)$$

\mathcal{K} projects from translational and rotational velocities of the rigid body to the translational velocities of the spherical subunits that constitute the body [33,58]. The rigid body mobility tensor, $\boldsymbol{\mu}$ [Eq. (1)], is calculated from \mathcal{M} as

$$\boldsymbol{\mu} = (\mathcal{K}^T \cdot \mathcal{M}^{-1} \cdot \mathcal{K})^{-1}. \quad (11)$$

III. SCALING APPROACH TO APPROXIMATE NEAR-WALL MOBILITY FUNCTIONS OF AN ARBITRARILY SHAPED BODY

The scaling approach to approximate near-wall mobilities of arbitrarily-shaped bodies proposed in the current work relies on theorems established by Hill and Power [35], and their application to energy dissipation in mobility problems by Kim and Karilla [36].

We start by considering two scenarios: a molecule suspended in an unbounded fluid and the same molecule suspended in a fluid bounded by a planar wall. Dissipation rates due to the motion of the molecule caused by an external force \mathbf{F} , satisfy [35,36]

$$E = \mathbf{F} \cdot \mathbf{V} \leq E_0 = \mathbf{F} \cdot \mathbf{V}_0, \quad (12)$$

where E_0 and E denote, respectively, dissipation rates in an unbounded fluid and in the fluid limited to a half space by a planar wall, $\mathbf{V}_0 = \boldsymbol{\mu}_0^{tt} \cdot \mathbf{F}$ is the translational velocity in an

unbounded fluid and $\mathbf{V} = \boldsymbol{\mu}^{tt} \cdot \mathbf{F}$ is the velocity near a planar boundary, $\boldsymbol{\mu}_0^{tt}$ is the translational block of the mobility tensor in an unbounded fluid, whereas $\boldsymbol{\mu}^{tt}$ is the translational block of the near-wall mobility tensor. The above inequality signifies that the presence of the wall results in a decrease in energy dissipation [35,36]. As the force acting on the molecule is arbitrarily chosen, one may conclude that for a force acting in the direction $\hat{\mathbf{e}}_i$, $i \in \{x, y, z\}$ the following relation holds for diagonal elements of translational blocks:

$$\mu_{ii}^{tt} \leq \mu_{0,ii}^{tt}. \quad (13)$$

For a molecule suspended either in an unbounded fluid or near a planar wall, under the influence of a nonzero external torque, \mathbf{T} , the following relation holds [35,36]:

$$E = \mathbf{T} \cdot \boldsymbol{\Omega} \leq E_0 = \mathbf{T} \cdot \boldsymbol{\Omega}_0. \quad (14)$$

$\boldsymbol{\Omega}_0 = \boldsymbol{\mu}_0^{rr} \cdot \mathbf{T}$ denotes the angular velocity in an unbounded fluid and $\boldsymbol{\Omega} = \boldsymbol{\mu}^{rr} \cdot \mathbf{T}$ is the angular velocity near a planar boundary, $\boldsymbol{\mu}_0^{rr}$ is the rotational block of the mobility tensor in an unbounded fluid whereas $\boldsymbol{\mu}^{rr}$ is the rotational block of the near-wall mobility tensor. Consequently, we have

$$\mu_{ii}^{rr} \leq \mu_{0,ii}^{rr}. \quad (15)$$

Let us now consider two representations of the same molecule: the detailed shell model, (s), and the coarse-grained model, for which fine details are lost at the benefit of computational efficiency (cg). We will use $\mu_{0,ii}^{\gamma,(s)}(\boldsymbol{\phi})$ and $\mu_{0,ii}^{\gamma,(cg)}(\boldsymbol{\phi})$, $\gamma \in \{tt, rr\}$ to denote bulk mobility coefficients of, respectively, the shell and the coarse-grained model. The index i corresponds to a particular direction, $\hat{\mathbf{e}}_i$, $i \in \{x, y, z\}$, in the laboratory frame. $\boldsymbol{\phi}$ is the orientation of the models, h is the distance to the boundary measured from the mobility center of the model. For orientation- and position-dependent near-wall mobility coefficients, we will use $\mu_{ii}^{\gamma,(s)}(h; \boldsymbol{\phi})$ and $\mu_{ii}^{\gamma,(cg)}(h; \boldsymbol{\phi})$. It is important to keep in mind that bulk coefficients, $\mu_{0,ii}^{\gamma}(\boldsymbol{\phi})$ are also limiting values of near-wall mobility functions, when molecule-wall separation tends to infinity

$$\mu_{ii}^{\gamma}(h; \boldsymbol{\phi}) \rightarrow \mu_{0,ii}^{\gamma}(\boldsymbol{\phi}) \quad \text{for } h \rightarrow \infty. \quad (16)$$

Mobilities $\mu_{ii}^{\gamma,(m)}(h; \boldsymbol{\phi})$, $m \in \{s, cg\}$ can be written as

$$\mu_{ii}^{\gamma,(m)}(h; \boldsymbol{\phi}) = \mu_{0,ii}^{\gamma,(m)}(\boldsymbol{\phi}) [1 - \delta_{ii}^{\gamma,(m)}(h; \boldsymbol{\phi})], \quad (17)$$

where $\delta_{ii}^{\gamma,(m)}(h; \boldsymbol{\phi})$ denotes the contribution resulting from the presence of the planar boundary which introduces an additional energy dissipation in the system; $\delta_{ii}^{\gamma,(m)}(h; \boldsymbol{\phi}) \geq 0$. We may thus write

$$\begin{aligned} \frac{\mu_{ii}^{\gamma,(s)}(h; \boldsymbol{\phi})}{\mu_{0,ii}^{\gamma,(s)}(\boldsymbol{\phi})} &= \frac{\mu_{ii}^{\gamma,(cg)}(h; \boldsymbol{\phi})}{\mu_{0,ii}^{\gamma,(cg)}(\boldsymbol{\phi})} \\ &\times \left[1 - \frac{\delta_{ii}^{\gamma,(s)}(h; \boldsymbol{\phi}) - \delta_{ii}^{\gamma,(cg)}(h; \boldsymbol{\phi})}{1 - \delta_{ii}^{\gamma,(cg)}(h; \boldsymbol{\phi})} \right]. \end{aligned} \quad (18)$$

If the molecule is sufficiently far from the wall so that lubrication effects play no role, then $1 - \delta_{ii}^{\gamma,(cg)}(h; \boldsymbol{\phi})$ is not close to zero and Eq. (18) is well-defined. Performing multipole expansion (B4) of the Blake tensor (B5) in the vicinity of the wall, we note that if the distance of the molecule from the wall is larger than its size, the presence of the image

molecule (located behind the wall) will affect only the lowest multipoles. These depend on the shape, size, and symmetry of the molecule [23] and can be tuned by appropriately choosing the coarse-grained model. We may thus expect that factors $\delta_{ii}^{\gamma,(cg)}(h; \boldsymbol{\phi})$ and $\delta_{ii}^{\gamma,(s)}(h; \boldsymbol{\phi})$ do not deviate significantly. As both quantities are positive, $|\delta_{ii}^{\gamma,(cg)}(h; \boldsymbol{\phi}) - \delta_{ii}^{\gamma,(s)}(h; \boldsymbol{\phi})|$ is at least an order of magnitude smaller than either $\delta_{ii}^{\gamma,(cg)}(h; \boldsymbol{\phi})$ or $\delta_{ii}^{\gamma,(s)}(h; \boldsymbol{\phi})$. This leads to the relation

$$\frac{\mu_{ii}^{\gamma,(s)}(h; \boldsymbol{\phi})}{\mu_{0,ii}^{\gamma,(s)}(\boldsymbol{\phi})} \approx \frac{\mu_{ii}^{\gamma,(cg)}(h; \boldsymbol{\phi})}{\mu_{0,ii}^{\gamma,(cg)}(\boldsymbol{\phi})} \quad (19)$$

and the conclusion that the ratio $\mu_{ii}^{\gamma,(m)}(h; \boldsymbol{\phi})/\mu_{0,ii}^{\gamma,(m)}(\boldsymbol{\phi})$ is much less sensitive to details of the molecular shape than $\mu_{ii}^{\gamma,(m)}(h; \boldsymbol{\phi})$ itself.

As a supplement to the above reasoning, we consider a capsule-like (i.e., shaped as a cylinder with hemispherical ends) molecule. Its shell and coarse-grained representations are shown in Fig. S2 [59]. Comparison of their bulk translational mobility coefficients (evaluated in body-fixed frames) gives $\mu_{0,11}^{tt,(s)}/\mu_{0,11}^{tt,(cg)} = \mu_{0,22}^{tt,(s)}/\mu_{0,2}^{tt,(cg)} = \mu_{0,33}^{tt,(s)}/\mu_{0,33}^{tt,(cg)} = 0.93$. In terms of re-creating mobility coefficients, the coarse-grained model is thus of a rather low quality. In Fig. S3 [59] we examine contributions to translational mobilities of both models resulting from the presence of the planar boundary, $\delta_{ii}^{tt,(m)}(h; \boldsymbol{\phi})$, $m \in \{s, cg\}$ [Eq. (17)]. As observed, for $h > L$, where L is the capsule long axis, the quantity $|\delta_{ii}^{tt,(cg)}(h; \boldsymbol{\phi}) - \delta_{ii}^{tt,(s)}(h; \boldsymbol{\phi})|$ is over an order of magnitude smaller than both $\delta_{ii}^{tt,(cg)}(h; \boldsymbol{\phi})$ and $\delta_{ii}^{tt,(s)}(h; \boldsymbol{\phi})$, thus the approximation [19] is justified.

In practical applications, Eq. (19) can be used to approximate near-wall position- and orientation-dependent mobilities of an arbitrarily shaped molecule, $\mu_{ii}^{\gamma,(s)}(h; \boldsymbol{\phi})$, using a very coarse, low-resolution representation of its shape, without the need to perform complicated calculations, simply by scaling the coarse-grained model mobility function, $\mu_{ii}^{\gamma,(cg)}(h; \boldsymbol{\phi})$, as

$$\mu_{ii}^{\gamma,(s)}(h; \boldsymbol{\phi}) \approx \frac{\mu_{0,ii}^{\gamma,(s)}(\boldsymbol{\phi})}{\mu_{0,ii}^{\gamma,(cg)}(\boldsymbol{\phi})} \mu_{ii}^{\gamma,(cg)}(h; \boldsymbol{\phi}). \quad (20)$$

The only requirement is that the bulk mobility tensor of the molecule, calculated accurately using a detailed model, is known. Mobility coefficients in an unbounded fluid, $\mu_{0,ii}^{\gamma,(s)}$ and $\mu_{0,ii}^{\gamma,(cg)}$, do not need to be recalculated each time the orientation is changed. One only needs to know $\boldsymbol{\mu}_0^{(s)}$ and $\boldsymbol{\mu}_0^{(cg)}$ either for a particular orientation in the laboratory frame or in the body-fixed frame, and then simply use an appropriate transformation matrix to obtain bulk mobilities for any $\boldsymbol{\phi}$.

As presented above, the scaling method can be applied directly to diagonal elements of the mobility matrix. However, approximation of the off-diagonal elements can also be achieved, although not directly. For instance, if one is interested in elements μ_{ij}^{tt} , $i \neq j$, scaling could be applied to elements

$$\begin{aligned} \mu_{+}^{tt} &= \frac{1}{\sqrt{2}}(\hat{\mathbf{e}}_i + \hat{\mathbf{e}}_j)^T \cdot \boldsymbol{\mu}^{tt} \cdot \frac{1}{\sqrt{2}}(\hat{\mathbf{e}}_i + \hat{\mathbf{e}}_j) \\ &= \frac{1}{2}(\mu_{ii}^{tt} + 2\mu_{ij}^{tt} + \mu_{jj}^{tt}) \end{aligned} \quad (21)$$

TABLE I. Bulk translational mobility coefficients of HEWL and DNA. Indices 11, 22, and 33 correspond to the directions of the axes of body-fixed frames (see Fig. 3). $\mu_0^{tt,(s)}$ is the isotropic translational mobility coefficient calculated as $\mu_0^{tt,(s)} = \frac{1}{3} \text{Tr}(\boldsymbol{\mu}_0^{tt,(s)})$.

	$\mu_{0,11}^{tt,(s)}/\mu_0^{tt,(s)}$	$\mu_{0,22}^{tt,(s)}/\mu_0^{tt,(s)}$	$\mu_{0,33}^{tt,(s)}/\mu_0^{tt,(s)}$
HEWL	0.97	0.98	1.05
DNA	0.92	0.92	1.16

and

$$\begin{aligned} \mu_{-}^{tt} &= \frac{1}{\sqrt{2}}(\hat{\mathbf{e}}_i - \hat{\mathbf{e}}_j)^T \cdot \boldsymbol{\mu}^{tt} \cdot \frac{1}{\sqrt{2}}(\hat{\mathbf{e}}_i - \hat{\mathbf{e}}_j) \\ &= \frac{1}{2}(\mu_{ii}^{tt} - 2\mu_{ij}^{tt} + \mu_{jj}^{tt}), \end{aligned} \quad (22)$$

as $\frac{1}{2}(\mu_{+}^{tt} - \mu_{-}^{tt}) = \mu_{ij}^{tt}$.

In a similar fashion, approximations to elements of the $\boldsymbol{\mu}^{tr}$ block can be obtained starting with a general relation for a molecule under the influence of both external force and torque [35,36]:

$$E = \mathbf{F} \cdot \mathbf{V} + \mathbf{T} \cdot \boldsymbol{\Omega} \leq E_0 = \mathbf{F} \cdot \mathbf{V}_0 + \mathbf{T} \cdot \boldsymbol{\Omega}_0 \quad (23)$$

or

$$\begin{pmatrix} \mathbf{F} \\ \mathbf{T} \end{pmatrix}^T \cdot \begin{pmatrix} \mu^{tt} & \mu^{tr} \\ \mu^{rt} & \mu^{rr} \end{pmatrix} \cdot \begin{pmatrix} \mathbf{F} \\ \mathbf{T} \end{pmatrix} \leq \begin{pmatrix} \mathbf{F} \\ \mathbf{T} \end{pmatrix}^T \cdot \begin{pmatrix} \mu_0^{tt} & \mu_0^{tr} \\ \mu_0^{rt} & \mu_0^{rr} \end{pmatrix} \cdot \begin{pmatrix} \mathbf{F} \\ \mathbf{T} \end{pmatrix}. \quad (24)$$

Any element of the $\boldsymbol{\mu}^{tr}$ block can be obtained using the procedure outlined in the case of μ_{ij}^{tt} , using a proper linear combinations of six-component vectors.

IV. APPLICATIONS—HEWL AND DNA

In this section, we demonstrate the application of the scaling approach to the calculation of diagonal elements of the near-wall mobility tensor. We consider two biomolecules: a typical globular protein hen egg-white lysozyme (HEWL, Fig. 1) and a 20 bp B-DNA duplex (DNA, Fig. 2). We also indirectly test the scaling hypothesis for off-diagonal elements by considering different orientations of molecules relative to the wall.

A. Hydrodynamic models

Two kinds of hydrodynamic representations of a molecular shape are used: a shell model, which consists of numerous spherical subunits and accounts for fine details of molecular shapes, and a coarse-grained model, in which the shape of the molecule is approximated with only a few spheres. The shell and coarse-grained models of HEWL and DNA are shown in Figs. 1 and S1 (HEWL) [59] and Fig. 2 (DNA). A detailed description of these models is given in the Appendices C and D. In all calculations, solvent viscosity was set to 0.89 mPa s.

B. Definition of the laboratory coordinate system

Except for the data presented in Tables I, II and Fig. S1 [59], mobility matrices were evaluated in the laboratory frame

TABLE II. Comparison of bulk mobilities obtained for shell (s) and coarse-grained (cg) models of HEWL and DNA. Indices 11, 22, and 33 correspond to the directions of the axes of body-fixed frames (see Fig. 3).

	$\mu_{0,11}^{tt,(s)}/\mu_{0,11}^{tt,(cg)}$	$\mu_{0,22}^{tt,(s)}/\mu_{0,22}^{tt,(cg)}$	$\mu_{0,33}^{tt,(s)}/\mu_{0,33}^{tt,(cg)}$
HEWL	1.02	1.01	1.03
DNA	0.99	0.99	1.00

consisting of three unit vectors $\{\hat{e}_{\parallel 1}, \hat{e}_{\parallel 2}, \hat{e}_{\perp}\}$, with the boundary in the plane spanned by $\hat{e}_{\parallel 1}$ and $\hat{e}_{\parallel 2}$ (see Fig. 3). The distance to the wall of a molecule is measured from its center of mobility.

The values presented in Tables I, II and Fig. S1 [59] correspond to the body-fixed frame, defined using the principal axes of the rotational block of the model mobility tensor.

The diagonal elements of the mobility matrices define the mobility coefficients with respect to the axes of the laboratory coordinate system. The bulk matrices and coefficients are denoted, respectively, by μ_0 and $\mu_{0,\parallel 1}^{\gamma}$, $\mu_{0,\parallel 2}^{\gamma}$ and $\mu_{0,\perp}^{\gamma}$, with $\gamma \in \{tt, rr\}$, whereas μ , $\mu_{\parallel 1}^{\gamma}$, $\mu_{\parallel 2}^{\gamma}$ and μ_{\perp}^{γ} are used for their near-wall counterparts.

C. Hydrodynamic calculations

Near-wall mobility tensors for shell and coarse-grained models, for different positions and orientations of molecules relative to the planar boundary, as well as bulk mobilities, were calculated numerically, using the *RigidMultiBlobsWall* package. In all calculations, and for both types of models, we consider only these molecule-wall configurations, for which the surface points of the model do not cross the wall. For shell models, the minimal gap between the model's surface and the bounding plane was roughly 3 Å.

Orientation-averaged mobilities were evaluated, for a given value of the molecule-wall distance, over an ensemble of 350

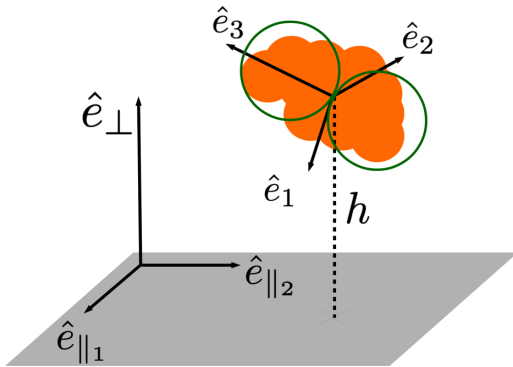


FIG. 3. Mobility coefficients of a given molecule, represented either with the shell (filled silhouette) or the coarse-grained model (empty circles) are calculated in the laboratory coordinate frame consisting of three unit vectors $\{\hat{e}_{\parallel 1}, \hat{e}_{\parallel 2}, \hat{e}_{\perp}\}$, with the boundary in the plane spanned by $\hat{e}_{\parallel 1}$ and $\hat{e}_{\parallel 2}$. Unit vectors $\{\hat{e}_1, \hat{e}_2, \hat{e}_3\}$ correspond to principal axes of the rotational block of the model mobility tensor and define the body-fixed frame. The distance to the wall of a molecule (h) is measured from its center of mobility.

orientations in the HEWL case, and over an ensemble of 500 orientations in the case of DNA. The orientations were generated using uniformly distributed random rotation matrices [62]. For each orientation of the molecule, a mobility tensor in the laboratory coordinate frame was calculated, and then all matrices were averaged over the orientations (error bars in the figures presented below correspond to standard deviations). Diagonal elements of the average matrix, $\bar{\mu}^{tt}$,

$$\bar{\mu}^{tt} = \bar{\mu}_{\perp}^{tt} \hat{e}_{\perp} \otimes \hat{e}_{\perp} + \bar{\mu}_{\parallel}^{tt} (\mathbf{I} - \hat{e}_{\perp} \otimes \hat{e}_{\perp}), \quad (25)$$

give the average translational mobility coefficients with respect to the axes of the laboratory coordinate system, $\bar{\mu}_{\parallel 1}^{tt} = \bar{\mu}_{\parallel 2}^{tt} = \bar{\mu}_{\parallel}^{tt}$ and $\bar{\mu}_{\perp}^{tt}$. The average mobilities depend on the position of the molecule relative to the wall.

D. Bulk mobility coefficients of HEWL and DNA

Translational mobility coefficients of HEWL and DNA in an unbounded fluid, calculated using the shell models, are given in Table I. We do not focus here on the determination of exact values of their bulk diffusion coefficients. Rather, we would like to demonstrate the link between the bulk and wall region mobilities. Precise calculations of the bulk mobilities might require the shell models to be constructed based on more detailed molecular representations than the one-bead-per-residue models that we use here, as well as accounting for specific and nonspecific hydration patterns [63–65]. Nevertheless, translational diffusion coefficients resulting from our calculations are in reasonable agreement with values reported in the literature. For HEWL our calculations result in a translational diffusion coefficient of roughly $12.6 \times 10^{-7} \text{ cm}^2/\text{s}$ that falls within the (adjusted for temperature) range of $11.5\text{--}14.9 \times 10^{-7} \text{ cm}^2/\text{s}$ reported in literature [66]. For the 20 bp DNA oligomer our calculations give the value of $12.9 \times 10^{-7} \text{ cm}^2/\text{s}$ that agrees with the experimentally determined value of $12.0 \times 10^{-7} \text{ cm}^2/\text{s}$ [67].

The comparison of the bulk mobility coefficients of HEWL and DNA, calculated for the shell and coarse-grained models (the dumbbell and the four-sphere model, respectively) is given in Table II. Although the HEWL dumbbell and the DNA four-sphere model are created solely based on very general geometric features of molecules, they perform quite well with regard to reproducing bulk mobilities obtained with detailed shell models. In the case of HEWL, mobility values obtained for the coarse-grained model are within 3% of the values calculated for the shell model. The corresponding number for DNA is 1%. Additionally, in Table S1 [59] we present a similar comparison for three-, six-, and nine-sphere models of HEWL. One may argue that these models do a better job at re-creating the complicated shape of HEWL, but their overall performance, considering bulk hydrodynamic properties, is worse than that of the dumbbell.

E. Near-wall orientation-averaged translational mobilities

Figures 4 and 5 show the comparison of the mobilities based on the orientation of the near wall of HEWL and DNA with the mobility functions of their equivalent spheres.

Both molecules and equivalent spheres are represented using shell models. As the hydrodynamic radius (R) of a given

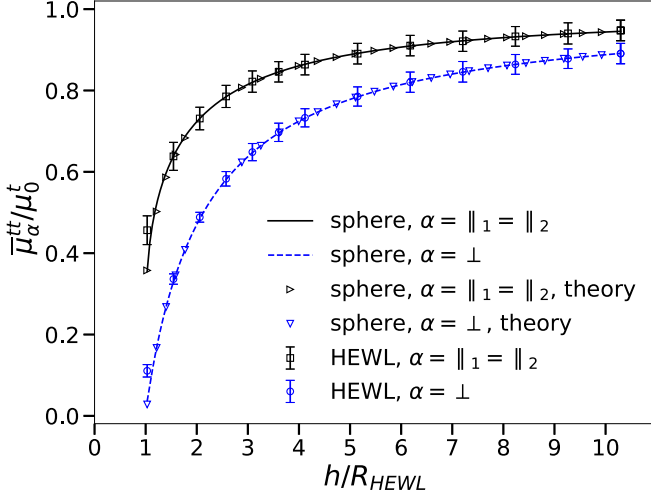


FIG. 4. Orientation-averaged translational mobility coefficients for HEWL, for motions in directions parallel and perpendicular to the wall, as functions of the HEWL-wall distance, compared with corresponding mobility coefficients of an equivalent sphere. Error bars correspond to standard deviations calculated over an ensemble of different orientations. For a comparison, we also show results (denoted *theory*) obtained using Eqs. (A1)–(A3).

object is related to its isotropic translational bulk mobility coefficient (μ_0^t) via

$$\mu_0^t = \frac{1}{3} \text{Tr}(\mu_0^{tt}) = (6\pi\eta R)^{-1}, \quad (26)$$

the bulk orientation-averaged mobility coefficient of a given molecule and the mobility coefficient of its equivalent sphere are equal. One may ask whether this equality of bulk mobilities results in a similar near-wall behavior of both objects, i.e., whether orientation-averaged mobilities of an anisotropic object can be effectively approximated by mobility functions

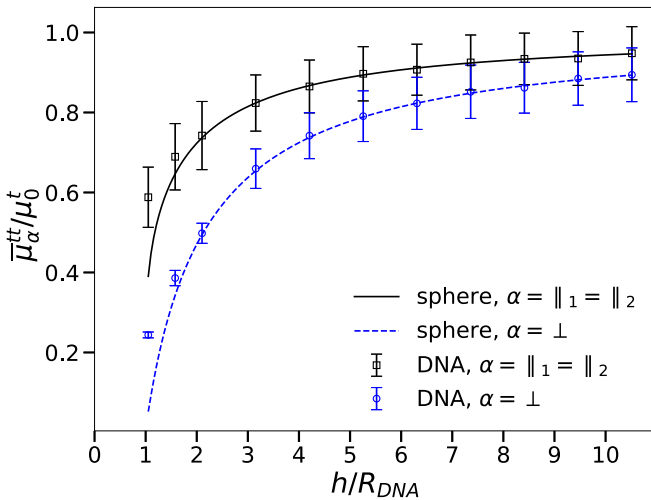


FIG. 5. Orientation-averaged translational mobility coefficients for DNA, for motions in directions parallel and perpendicular to the wall, as functions of the DNA-wall distance, compared with corresponding mobility coefficients of an equivalent sphere. Error bars correspond to standard deviations calculated over an ensemble of different orientations.

of a spherical particle. The answer to this question is not obvious, as hydrodynamic interactions between an anisotropic object and the boundary are not only position- but also orientation-dependent, and thus results of averaging over different orientations cannot be straightforwardly predicted. For both HEWL (Fig. 4) and DNA (Fig. 5) there is a perfect agreement of near-wall orientation-averaged mobilities with mobilities of equivalent spheres, at all molecule-wall separations for which molecules are free to rotate without the steric impediment of the wall. It thus appears that as far as the orientation-averaged mobilities are considered, the shape of the molecule does not matter. However, once steric interactions come into play and some orientations of molecules are prohibited, the mobilities diverge. In particular, close to the plane, steric interactions preclude these orientations in which long molecular axes are perpendicular to the wall.

The results shown in Figs. 4 and 5 conform to the following relation:

$$\frac{\bar{\mu}_\alpha^{tt,(\text{molecule})}(h)}{\mu_0^{t,(\text{molecule})}} \approx \frac{\mu_\alpha^{tt,(\text{sphere})}(h)}{\mu_0^{t,(\text{sphere})}} \quad \text{for } \alpha \in \{\parallel, \perp\}, \quad (27)$$

where α denotes the direction relative to the wall. Obviously, the above expression does not hold close to the boundary because of orientational constraints imposed by the wall. Moreover, there are scenarios where the spherical approximation would not be really useful. One example is the diffusion of an elongated object (such as the DNA oligomer) under confinement. Another possible example is a molecule characterized by an anisotropic charge distribution, forced into a particular orientation relative to the boundary by an external electric field. In such scenarios, the molecule is not able to rotate freely and thus the complete orientation averaging of its translational mobilities cannot be achieved, rendering the spherical approximation useless. All this could perhaps be remedied by replacing the sphere with an object that is better suited to represent an actual molecular shape yet is still simple enough for efficient numerical, or even analytical calculations, such as one of the coarse-grained models presented in Figs. 1, 2, and S1 [59]. We will explore and test this idea in the next section, where we benchmark approximate near-wall mobility functions of HEWL and DNA calculated according to Eq. (20) against the results of the shell models.

F. Approximation for near-wall mobility functions of arbitrarily shaped molecules

With an axial ratio of roughly 1.5 (Table III) HEWL has a moderately elongated shape, and as a consequence its near-wall mobilities depend not only on its position but also on its orientation. Consequently, results of a direct (i.e., not involving scaling) comparison of perpendicular and parallel mobilities of differently oriented HEWL with mobility functions of a sphere with the same hydrodynamic radius are not very encouraging. For example, in Figs. 6 (left panel) and S4 [59] mobility functions of HEWL oriented either perpendicular or parallel to the wall are plotted against the mobilities of a sphere. Hydrodynamic anisotropy of the protein is clearly visible, and it appears that the equivalent sphere is a rather poor approximation of HEWL shape. However, if we consider

TABLE III. Details of HEWL and DNA hydrodynamic models. R - hydrodynamic radius of the molecule resulting from calculations performed for its shell model; hydrodynamic radius calculated for the spherical shell representing the equivalent sphere is given within parentheses. L , maximal dimension along the long axis of the molecule (calculated for its bead model). d , diameter of the molecule (calculated for its bead model). $N^{(s)}$, number of elements in the shell model. $r^{(s)}$, radius of spherical elements in the shell model; radius of spherical subunits in the equivalent sphere model is given within parentheses. $r^{(cg)}$, radius of spherical subunits in the coarse-grained model of the molecule.

	R [Å]	L [Å]	d [Å]	$N^{(s)}$	$r^{(s)}$ [Å]	$r^{(cg)}$ [Å]
HEWL	19.42 (19.43)	52.92	34.18	18 213	0.29 (0.33)	17.09
DNA	19.03 (19.02)	74.60	20.1	14 618	0.33 (0.32)	10.05

the sphere as a coarse-grained model of HEWL and scale the sphere mobility functions according to expression 20, then they agree much better with accurate (i.e., calculated using the shell model) HEWL mobilities (right panel of Figs. 6 and S5 [59]), particularly for protein-wall distances greater than roughly three times the HEWL hydrodynamic radius. Below this threshold, scaled mobility functions progressively deviate from those calculated for the fine model. The largest deviations are observed for parallel components of mobilities and for HEWL oriented either parallel or perpendicular to the wall, whereas the approximation 20 works best for HEWL tilted toward the wall.

A much better representation of the anisotropic HEWL shape is achieved with a dumbbell (Fig. 1). Consequently, apart from relatively small molecule-wall distances at which fine details of HEWL molecular shape and lubrication effects come into play, scaled dumbbell mobility functions are in an almost perfect agreement with HEWL mobilities, regardless of the molecule orientation (Fig. 7).

The results obtained for the three-, six-, and nine-sphere HEWL models are presented in Figs. S6, S7, and S8 [59]. One may expect, that as the number of spheres in the model increases and, at the same time, spheres get smaller (see the caption for Fig. S1 [59]) the scaling approach should perform better at smaller distances from the wall. Indeed, close to the wall, the best agreement of scaled mobilities with those

calculated for the shell model is obtained with the nine-sphere model. For the comparison sake, in Fig. S9 [59] we show nonscaled translational mobilities of the nine-sphere model against mobilities of the shell model. Clearly, without the scaling, the nine-sphere model performs rather poorly.

In the case of the 20 bp DNA oligomer, whose coarse-grained model consists of four overlapping spheres (Fig. 2) the scaling approach performs very well, again failing only at very small molecule-wall separations (Fig. 8).

The approach based on approximation (20) can also be applied to evaluate rotational mobility functions of arbitrarily shaped objects, with a small subtlety, as discussed below. Consider the axisymmetric coarse-grained models of HEWL and DNA utilized in the current work. Because their mobility tensors are derived from the $3N \times 3N$ translational part of the RPY tensor [Eqs. (3), (4), and (11)], mobility coefficients for rotations about their long axes are not properly defined. Only the spheres positioned off the rotation axis give rise to the rotations of the rigid body. There are two ways to remedy this problem. The first is to use the $6N \times 6N$ RPY tensor that includes the rotations of the spheres that make up the bodies and the couplings between their translations and rotations [38,68]. The second, less optimal from the point of view of computational efficiency, is to consider coarse-grained models consisting of a larger number of subunits, such as the three-, six-, and nine-sphere HEWL models (Fig. S1 [59]).

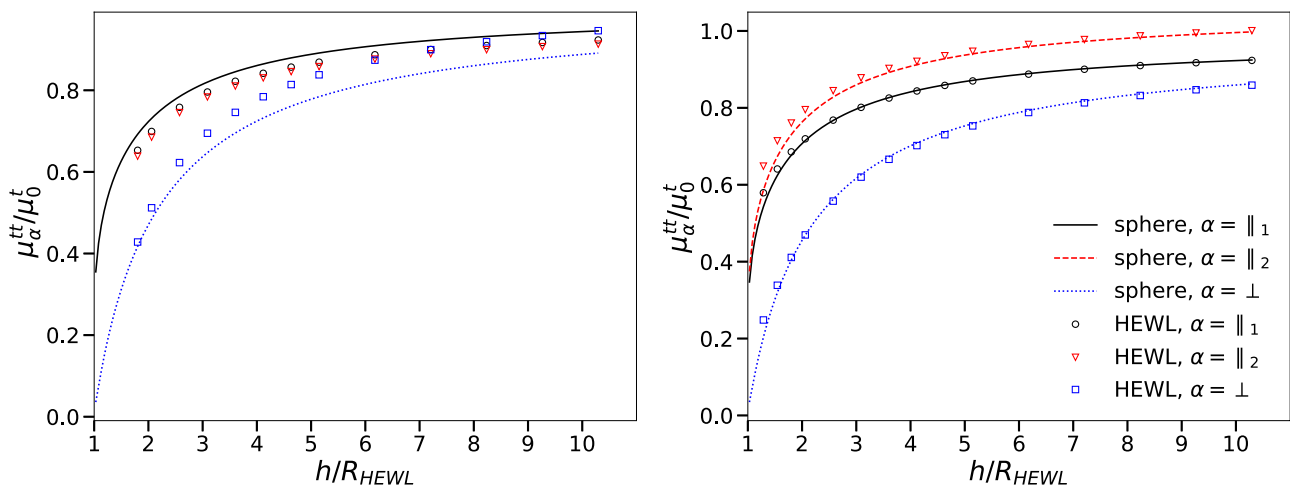


FIG. 6. Left panel: Translational mobilities calculated for the HEWL shell model, for motions in directions parallel and perpendicular to the wall, compared with mobilities of an equivalent sphere. Right panel: HEWL translational mobilities, for motions in directions parallel and perpendicular to the wall, compared with scaled mobilities of an equivalent sphere. Data presented in both panels is for HEWL long axis oriented parallel to the wall.

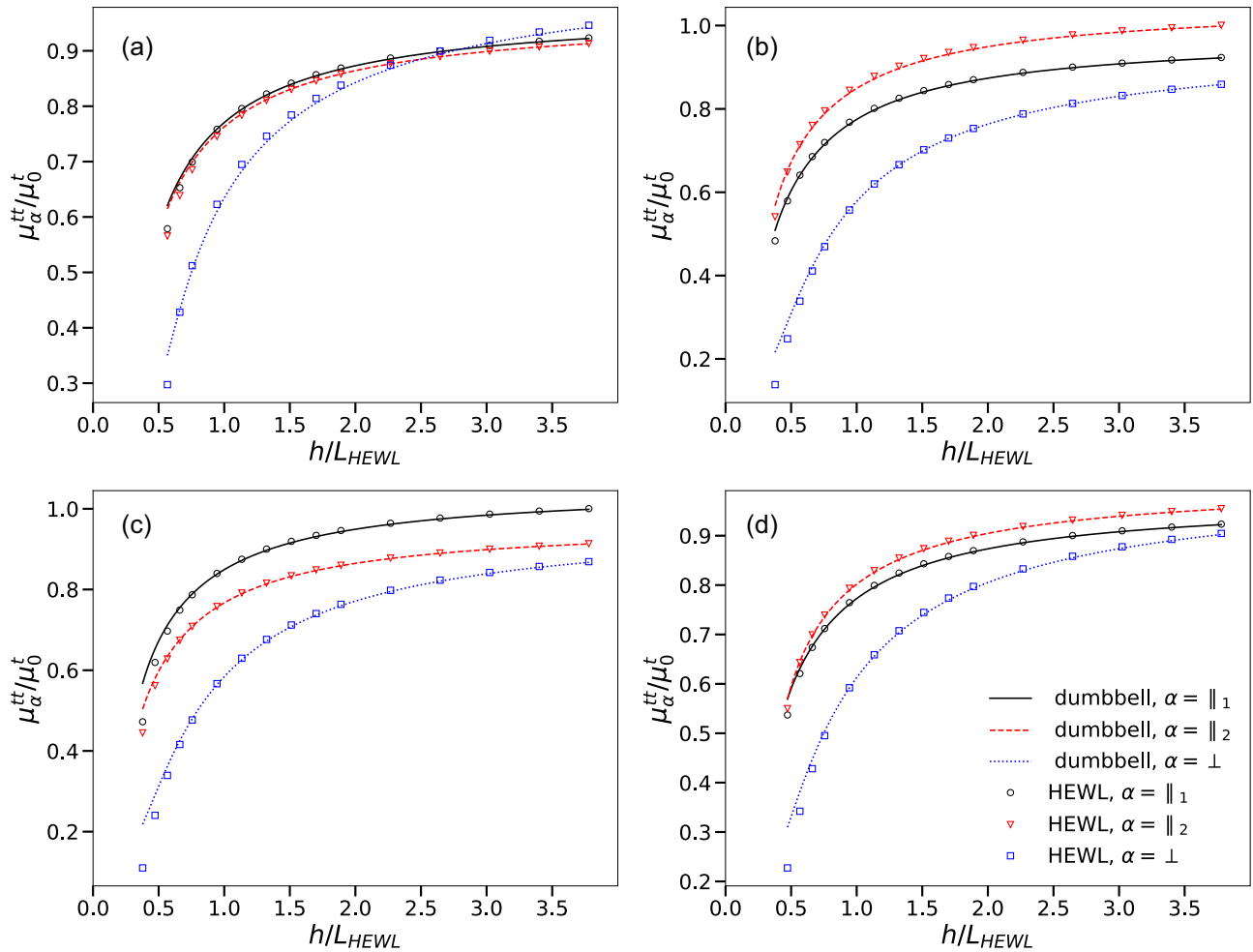


FIG. 7. Translational mobilities calculated for the HEWL shell model, for motions in directions parallel and perpendicular to the wall, as functions of the HEWL-wall distance, compared with scaled mobilities of a dumbbell. (a) HEWL long axis perpendicular to the wall. (b) HEWL long axis parallel to the wall (the molecule is rotated around the first principal axis of the rotational diffusion tensor, perpendicular to the long axis). (c) HEWL long axis parallel to the wall (the molecule is rotated around the second principal axis of the rotational diffusion tensor, perpendicular to the long axis). (d) HEWL long axis inclined at 45 degrees angle to the wall.

In Figs. 9 and 10 we show, respectively, the scaled rotational mobility functions of the HEWL dumbbell and the DNA four-sphere model, compared with the mobility functions of the shell models. We consider molecule-plane configurations in which the long axis of the molecule is either perpendicular or parallel to the plane and evaluate, where possible, rotations about directions $\{\hat{e}_{\parallel_1}, \hat{e}_{\parallel_2}, \text{ and } \hat{e}_{\perp}\}$ (Fig. 3). For both molecules, the scaling approach performs to our satisfaction, especially considering that coarse-grained models rather poorly reproduce the bulk rotational diffusivities of shell models (the relative difference is roughly 20% for HEWL and roughly 10% for DNA).

As mentioned above, all HEWL rigid-body rotations can be resolved with three-, six-, and nine-sphere coarse-grained models. Their scaled rotational mobility functions are shown in Figs. S10, S11, and S12 [59], whereas their performance with regard to re-creating bulk rotational diffusivities of shell models can be judged based on data given in Table S1 [59]. Again, close to the wall, the scaled mobility functions of the nine-sphere model are in the best agreement with corresponding functions of the shell model.

G. Range of validity

We used data obtained for different coarse-grained HEWL models (i.e., the dumbbell and three-, six-, and nine-sphere models) to estimate the range of validity of the scaling approach when applied to evaluate near-wall translational and rotational mobilities. For that, we calculated the relative differences between the mobility functions of the shell model and the scaled functions of the coarse-grained models. These differences are shown in Figs. S13 (translations) and S14 (rotations) [59] as functions of the molecule-wall distance. It is apparent that for both translational and rotational motions, the scaling approach performs very well for distances between the center of the molecule and the wall greater than the HEWL diameter (which is actually rather close to the wall in terms of the surface-surface distance; the reader may recall that the axial ratio of lysozyme is 1.5). The differences between accurate and approximate functions are no greater than 10%, which is perfectly adequate given other approximations which are usually incurred in hydrodynamic modeling (e.g., a simplified representation of the hydration layer). As expected, the larger the molecule-wall distance, the smaller the difference.

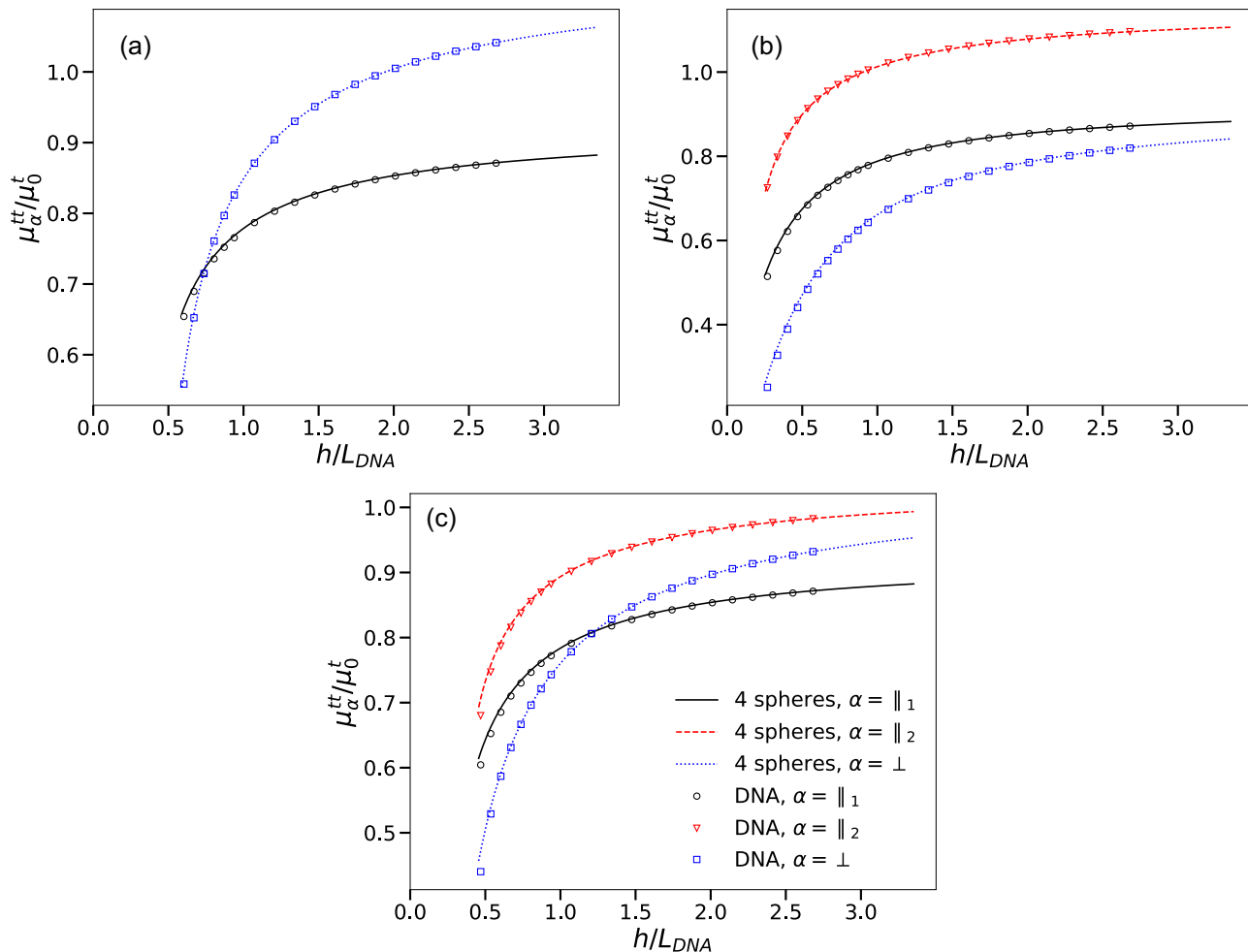


FIG. 8. Translational mobilities calculated for the DNA shell model, for motions in directions parallel and perpendicular to the wall, as functions of the DNA-wall distance, compared with scaled mobilities of the four-sphere model. (a) DNA long axis perpendicular to the wall. (b) DNA long axis parallel to the wall. (c) DNA long axis inclined at 45 degrees angle to the wall.

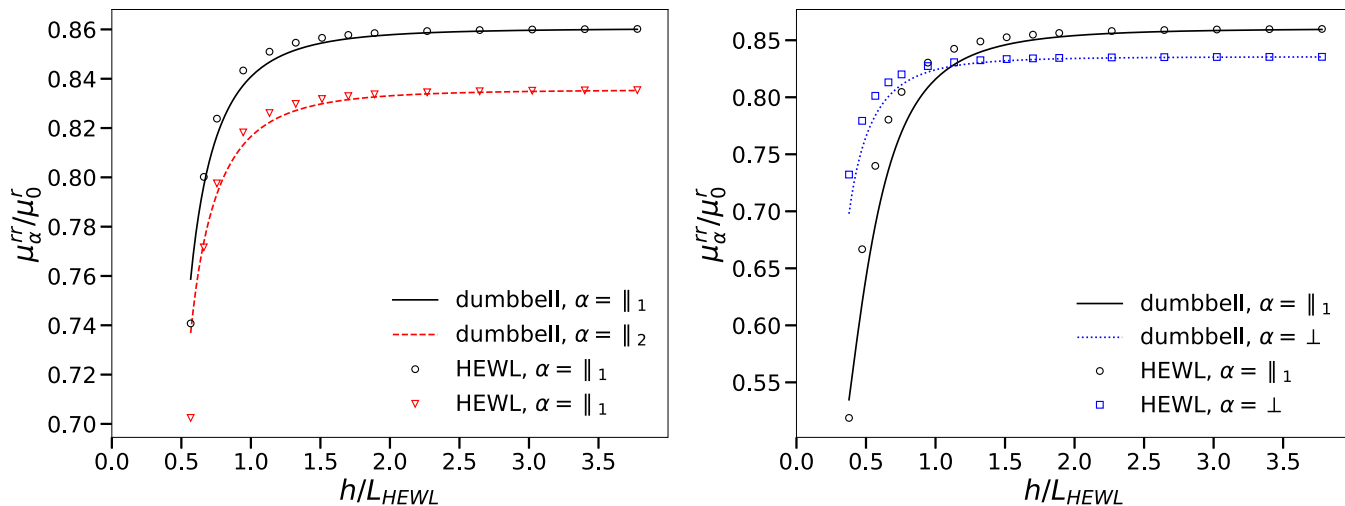


FIG. 9. Rotational mobility functions calculated for the HEWL shell model, for rotations about axes parallel and perpendicular to the wall, compared with scaled rotational mobility functions of the dumbbell. Left panel: HEWL long axis perpendicular to the wall. Right panel: HEWL long axis parallel to the wall. μ_0^r is the bulk rotational mobility coefficient of HEWL calculated based on its hydrodynamic radius, R , as $\mu_0^r = (8\pi\eta R^3)^{-1}$.

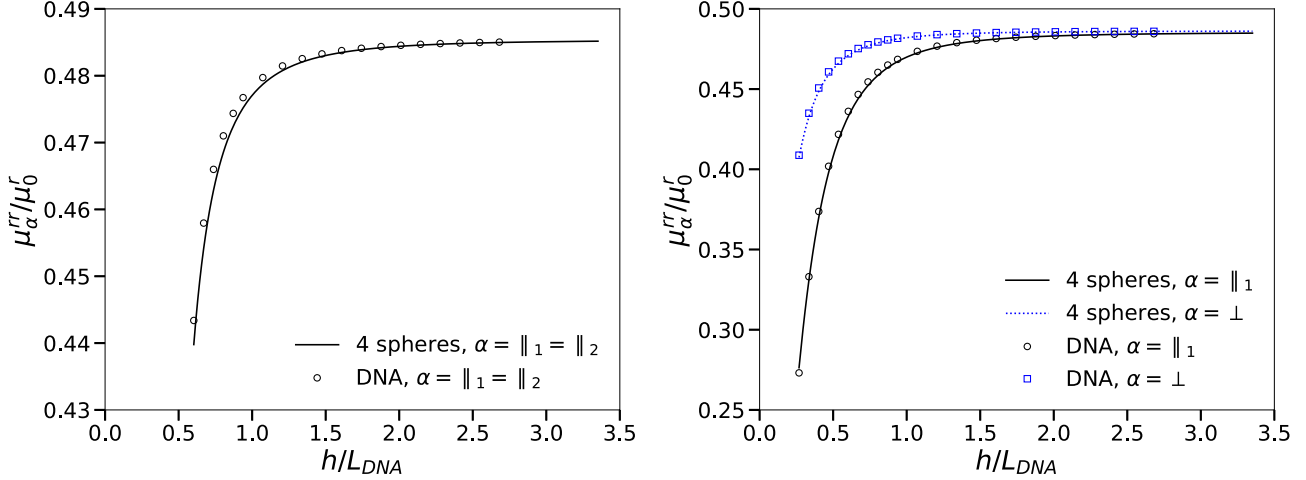


FIG. 10. Rotational mobility functions calculated for the DNA shell model, for rotations about axes parallel and perpendicular to the wall, compared with scaled rotational mobility functions of the four-sphere model. Left panel: DNA long axis perpendicular to the wall. Right panel: DNA long axis parallel to the wall. μ_0^r is the bulk rotational mobility coefficient of DNA calculated based on its hydrodynamic radius, R , as $\mu_0^r = (8\pi\eta R^3)^{-1}$.

For molecule-wall distances below the molecule diameter, the agreement rapidly becomes worse. There are two reasons for this. The first is related to the lack of fine molecular details in the coarse-grained models. The second is related to the lubrication effects, which are not accounted for in the coarse-grained models. For the shell model, this problem is somewhat alleviated by using small spheres.

Note that the failure of the scalings in the immediate vicinity of the wall is not necessarily a detriment since these length scales are beyond the range of applicability of coarse-grained models anyway. Dynamics in this regime should be investigated using an atomistic rather than coarse-grained description of the molecule-wall system.

V. CONCLUSION

Based on the extremum principles for Stokes flows produced by the motion of rigid bodies, we have developed a scaling method that can be used to construct approximate mobility functions of arbitrarily shaped rigid molecules near a planar wall. In our approach, molecular shapes are constructed from a few spheres and hydrodynamic interactions are evaluated using the Rotne-Prager-Yamakawa tensor corrected for system boundaries. Low resolution of the models, together with the RPY-level description of hydrodynamic interactions, make the approach very efficient from the computational standpoint. Consequently, it can be utilized in dynamical simulations in which repetitive, on-the-fly calculations of position- and orientation-dependent mobilities are necessary. The computational efficiency of the model is demonstrated in

Fig. S15 [59] showing how the time needed to evaluate the mobility tensor matrix scales with the number of subunits in the hydrodynamic model. The benefit of using low-resolution models, in terms of calculation time, is substantial. Despite the relative simplicity of the models and low-level description of hydrodynamic interactions, the presented approach is still accurate enough to capture the dynamics of molecules suspended close to the planar boundary. We presume that the described method can be applied to more complicated geometries. For that, one needs to use a generalization of the RPY tensor applicable for a given confinement geometry [38] and choose a proper reference point. Here, we used a point located at an infinite distance from the plane. In a general case, one should simply select as the reference the point in space in which the effect of boundaries is minimal. For example, for the molecule moving between two planar walls, the proper choice would be the position in the middle between them [69]. This issue will be the subject of a future investigation.

ACKNOWLEDGMENT

M.D. acknowledges support from National Science Centre, Poland (Grant No. UMO-2016/23/B/ST4/03273).

APPENDIX A: NEAR-WALL MOBILITY OF A SPHERE

Brenner derived an exact solution for the drag acting on a sphere moving in the direction perpendicular to the wall [16], resulting in the following formula for the sphere translational mobility coefficient as a function of the sphere-wall distance

$$\mu_{\perp}^t(h) = \frac{1}{6\pi\eta a} \left(\frac{4}{3} \sinh(\alpha) \sum_{n=1}^{\infty} \frac{n(n+1)}{(2n-1)(2n+3)} \left\{ \frac{2 \sinh[(2n+1)\alpha] + (2n+1) \sinh(2\alpha)}{4 \sinh^2[(n+\frac{1}{2})\alpha] - (2n+1)^2 \sinh^2(\alpha)} - 1 \right\} \right)^{-1}, \quad (\text{A1})$$

where $\alpha = \cosh^{-1}(\frac{h}{a})$.

For motion in the direction parallel to the wall, numerical representations of the mobility function, accurate at all sphere-wall separations, are available [70,71]. DeLong *et al.* [53] obtained an approximate form of $\mu_{\parallel}(h)$ by combining the near-wall expression derived by Goldman and Brenner [15]

$$\mu_{\parallel}^{tt}(h) \approx \frac{1}{6\pi\eta a} \frac{2[\ln(\frac{h}{a} - 1) - 0.9543]}{[\ln(\frac{h}{a} - 1)]^2 - 4.325 \ln(\frac{h}{a} - 1) + 1.951}$$

for $\frac{h}{a} \leq 1.03$, (A2)

with a power series expansion in the inverse of h , truncated to the fifth order [28]

$$\mu_{\parallel}^{tt}(h) \approx \frac{1}{6\pi\eta a} \left(1 - \frac{9a}{16h} + \frac{a^3}{8h^3} - \frac{45a^4}{256h^4} - \frac{a^5}{16h^5} \right)$$

for $\frac{h}{a} > 1.03$. (A3)

APPENDIX B: MULTIPOLE EXPANSION

In an unbounded space, due to the linearity of the Stokes equations, the relation between the flow disturbance created by a moving biomolecule and induced force density localized on the molecule surface can be written as [72]

$$\mathbf{v}(\mathbf{r}) = - \int \mathbf{T}(\mathbf{r} - \mathbf{r}') \cdot \mathbf{f}(\mathbf{r}') d^3\mathbf{r}', \quad (\text{B1})$$

where $\mathbf{f}(\mathbf{r}')$ is the density of hydrodynamic drag forces acting on a molecule. The hydrodynamic Green function, \mathbf{T} , is given by the Oseen tensor

$$\mathbf{T}(\mathbf{r}) = \frac{1}{8\pi\eta r} (\mathbf{1} + \hat{\mathbf{r}}\hat{\mathbf{r}}). \quad (\text{B2})$$

At large distances from a biomolecule Eq. (B1) simplifies to

$$\mathbf{v}(\mathbf{r}) = -\mathbf{T}(\mathbf{r}) \cdot \mathbf{F}, \quad (\text{B3})$$

where \mathbf{F} is the total hydrodynamic drag on a molecule and \mathbf{r} is calculated with respect to the origin located inside the molecule. The above relation is analogous to electrostatics, where an electric field generated by a distribution of charges reduces at large distances to that of a point charge. Similarly, in Eq. (B3) the flow field at large distances becomes independent of the details of the particle shape. In a similar vein to the electrostatic problem, one can now introduce the multipole expansion by expanding $\mathbf{T}(\mathbf{r} - \mathbf{r}')$ into a Taylor series in \mathbf{r}' around $\mathbf{r}' = 0$ [44]:

$$\mathbf{T}(\mathbf{r} - \mathbf{r}') = \sum_{n=1}^{\infty} \frac{(-1)^n}{n!} (\mathbf{r}' \cdot \nabla)^n \mathbf{T}. \quad (\text{B4})$$

Inserting the expansion into Eq. (B1) leads to the representation of the flow field as a series in $\frac{1}{r}$, analogous to the multipole expansion in electrostatics. At large distances from the molecule, only the lowest multipoles (which depend on its shape, size, and symmetry) play a role in determining the flow field: a monopole term, called the Stokeslet, that decays as r^{-1} , as well as a force dipole term (Stokes doublet) that decays as r^{-2} . The dipole term can be split into a symmetric part (stresslet) and an antisymmetric part (rotlet).

In the presence of the bounding wall, the Green function needs to be modified, by adding an extra term, $\mathbf{T}_{im}(\mathbf{r}, \tilde{\mathbf{r}}')$ with the additional force multipoles located at $\tilde{\mathbf{r}}'$ —the mirror image position of $\tilde{\mathbf{r}}$ on the other side of the boundary. As derived by Blake [39],

$$\mathbf{T}_B(\mathbf{r}, \mathbf{r}') = \mathbf{T}(\mathbf{r} - \mathbf{r}') + \mathbf{T}_{im}(\mathbf{r}, \tilde{\mathbf{r}}'). \quad (\text{B5})$$

The image system involves a Stokeslet with an opposite sign, as well as the stresslet and the sourcelet [39]. The flow field can then again be calculated by a relation analogous to Eq. (B1), this time involving $\mathbf{T}_B(\mathbf{r}, \mathbf{r}')$.

APPENDIX C: SHELL MODELS OF HEWL AND DNA

The procedure applied to construct shell models of molecules follows the general approach outlined by de la Torre *et al.* [41], in which one starts with atomic coordinates of molecules and replace either atoms or groups of atoms (residues) with spherical elements/beads of fixed radius. The resulting primary model is in turn represented by a shell model. Primary models constructed in the current work are of the one-bead-per-residue variety [73–75].

Hen egg-white lysozyme shell model was created based on atomic coordinates stored in the Protein Data Bank [76] under the accession code 6LYZ [60] (Fig. 1) according to the following procedure.

First, a bead representation of HEWL was built, with spherical elements (beads) positioned at geometric centers of its amino acids. Each bead was assigned a radius computed as the mean maximal distance of any heavy atom of a given amino acid from the center of its bead, increased by the radius of a water molecule (1.4 Å). The resulting model of HEWL consists of 129 beads with radii of 4.24 Å (Fig. 1). In the second step, each bead in the model was replaced with a spherical shell, of the same radius, whose surface is covered with 642 small spheres, distributed according to the algorithm described by Usabiaga *et al.* [33], that we describe here only briefly. The authors start with 12 small spheres assigned to vertices of an isosahedron, which results in a uniform triangulation of a sphere by 20 faces. Next, they place a new sphere at the center of each edge and recursively subdivide each triangle into four smaller triangles, projecting the vertices back to the surface of the spherical shell along the way. After each subdivision, the number of vertices is approximately quadrupled and after the fourth subdivision the number of spheres is 642 [33]. The radius of small spheres on the surface of each spherical shell is set to the half of the minimal spacing between any two of them. Small spheres that are not accessible from the outside of the molecule are removed from its final shell model (Fig. 1, Table III).

An equivalent sphere of lysozyme, i.e., a sphere having the same hydrodynamic radius as the HEWL shell model, consist of 10 242 spherical subunits distributed on the surface of a sphere with the radius (resulting from an iterative optimization procedure) of 19.32 Å. Again, the radius of small spheres is set to the half of the minimal spacing between any two of them.

The shell model of the 20 bp DNA B-helix (Fig. 2) was created based on atomic coordinates generated with the AmberTools suite [77,78] using the same procedure as the one

applied to the HEWL molecule. In the bead model spherical subunits are positioned at geometric centers of nucleotides and their radius is calculated as the mean maximal distance of any heavy atom of a given nucleotide, from the center of its bead, increased by the radius of a water molecule. The resulting model of DNA consisted of 40 beads with radii of 4.42 Å. Each bead was replaced with a spherical shell covered with 642 spherical subunits, from which only the ones accessible from the outside of the molecule are retained in the final shell model (Fig. 2, Table III).

An equivalent sphere of DNA consist of 10 242 spherical subunits distributed on the surface of a sphere with the radius of 18.91 Å.

Coordinates of the spheres that constitute the shell model of a given molecule were transformed to the body-fixed frame with the origin located at the mobility center, using equations given in Refs. [55,79], whose axes coincide with the principal axes of the rotational block of the model mobility tensor. Coordinate manipulations were performed using an in-house software.

Spherical shells covered with different numbers of spherical subunits were generated using tools provided with the *RigidMultiBlobsWall* package. Shell models of HEWL and DNA were created using an in-house software.

APPENDIX D: COARSE-GRAINED MODELS OF HEWL AND DNA

Coarse-grained models of molecules are not uniquely defined, and different approaches can be taken to build them. Ideally, the level of details of the molecular shape in the coarse-grained model should be as low as possible to maximize the speed of hydrodynamic calculations. The features of a molecule that one should consider creating its coarse-grained model are the size, shape, and symmetry.

Both HEWL and DNA are aspherical molecules. HEWL shape is the more complicated of the two. HEWL is rather globular yet fully anisotropic (Fig. 1) and contains a large cavity able to accommodate quite sizable ligands [80]. However, the elongated shape of the 20 bp DNA oligomer is

quite regular, with two grooves, minor and mayor, forming helical paths along the long axis of the molecule and giving rise to the rotational pseudosymmetry. In the first (and very crude) approximation, both HEWL and DNA can be treated as axially symmetric bodies whose sizes can be estimated from appropriate bounding boxes enclosing their molecular shapes. Hence, the coarse-grained HEWL model consists of two overlapping spheres that form a dumbbell (Fig. 1, Table III). The radius of spheres and the distance between their centers are chosen in such a manner that the length of the dumbbell and its diameter correspond to maximal dimensions of the shell HEWL model along directions of principal axes of the rotational block of the mobility tensor (the diameter of the dumbbell is calculated as an average of maximal dimensions of HEWL along directions perpendicular to its long axis). Similarly, the coarse-grained model of the 20 bp DNA oligomer consists of four, equally spaced, overlapping spheres (Fig. 2, Table III) whose positions and dimensions are derived from the dimensions of the shell model of the molecule.

As we have stated above, there is a latitude in the definition of a coarse-grained model. To expand on this issue and at the same time to show that the process of building a coarse-grained model can be automated, in the HEWL case we considered three additional coarse-grained models created based on the shape-based coarse-graining (SBCG) algorithm authored by Arkhipov, Fredolino and Schulten [81] implemented in the VMD package [82]. These models consist of three, six, and nine spheres (Fig. S1 [59]). Positions of spheres within each model are calculated based on the PDB structure of HEWL [60] using the SBCG algorithm. For each model, identical radii of spheres are chosen in such a way that the dimensions of the coarse-grained and the shell model along the direction of the longest principal axis of the rotational block of the mobility tensor are equal.

As in the case of shell models, coordinates of all coarse-grained models were transformed to the body-fixed frame, whose axes are the principal axes of the rotational block of the mobility tensor and origin coincides with the mobility center.

-
- [1] J. K. Pero, E. M. Haas, and N. L. Thompson, Size dependence of protein diffusion very close to membrane surfaces: Measurement by total internal reflection fluorescence correlation spectroscopy, *J. Phys. Chem. B* **110**, 10910 (2006).
- [2] E. M. Smith, J. Hennen, Y. Chen, and J. D. Mueller, *In situ* quantification of protein binding to the plasma membrane, *Biophys. J.* **108**, 2648 (2015).
- [3] M. Ozboyaci, D. B. Kokh, and R. C. Wade, Three steps to gold: Mechanism of protein adsorption revealed by Brownian and molecular dynamics simulations, *Phys. Chem. Chem. Phys.* **18**, 10191 (2016).
- [4] R. L. Williams and D. F. Williams, Albumin adsorption on metal surfaces, *Biomaterials* **9**, 206 (1988).
- [5] P. Mereghetti and R. C. Wade, Diffusion of hydrophobic proteins in solution and interactions with a graphite surface, *BMC Biophys.* **4**, 9 (2011).
- [6] B. Fair and A. Jamieson, Studies of protein adsorption on polystyrene latex surfaces, *J. Colloid Interface Sci.* **77**, 525 (1980).
- [7] E. Kätelhön, S. V. Sokolov, and R. G. Compton, Near-wall hindered diffusion: Implications for surface-based sensors, *Sens. Actuat. B: Chem.* **234**, 420 (2016).
- [8] T. M. Squires, R. J. Messinger, and S. R. Manalis, Making it stick: Convection, reaction, and diffusion in surface-based biosensors, *Nat. Biotechnol.* **26**, 417 (2008).
- [9] D. Keng, S. R. McAnanama, I. Teraoka, and S. Arnold, Resonance fluctuations of a whispering gallery mode biosensor by particles undergoing Brownian motion, *Appl. Phys. Lett.* **91**, 103902 (2007).
- [10] K. D. Dorfman, D. Gupta, A. Jain, A. Muralidhar, and D. R. Tree, Hydrodynamics of DNA confined in nanoslits and nanochannels, *Eur. Phys. J.: Spec. Top.* **223**, 3179 (2014).

- [11] J. S. Lee, E. Um, J. Park, and C. B. Park, Microfluidic self-assembly of insulin monomers into amyloid fibrils on a solid surface, *Langmuir* **24**, 7068 (2008).
- [12] A. Aksimentiev, Deciphering ionic current signatures of DNA transport through a nanopore, *Nanoscale* **2**, 468 (2010).
- [13] M. Wanunu, J. Sutin, B. McNally, A. Chow, and A. Meller, DNA translocation governed by interactions with solid-state nanopores, *Biophys. J.* **95**, 4716 (2008).
- [14] M. Reinhardt, N. J. Bruce, D. B. Kokh, and R. C. Wade, Brownian dynamics simulations of proteins in the presence of surfaces: Long-range electrostatics and mean-field hydrodynamics, *J. Chem. Theory Comput.* **17**, 3510 (2021).
- [15] A. J. Goldman, R. G. Cox, and H. Brenner, Slow viscous motion of a sphere parallel to a plane wall: I. Motion through a quiescent fluid, *Chem. Eng. Sci.* **22**, 637 (1967).
- [16] H. Brenner, The slow motion of a sphere through a viscous fluid towards a plane surface, *Chem. Eng. Sci.* **16**, 242 (1961).
- [17] P. Holmqvist, J. K. G. Dhont, and P. R. Lang, Anisotropy of Brownian motion caused only by hydrodynamic interaction with a wall, *Phys. Rev. E* **74**, 021402 (2006).
- [18] P. Huang and K. S. Breuer, Direct measurement of anisotropic near-wall hindered diffusion using total internal reflection velocimetry, *Phys. Rev. E* **76**, 046307 (2007).
- [19] A. Banerjee and K. D. Kihm, Experimental verification of near-wall hindered diffusion for the Brownian motion of nanoparticles using evanescent wave microscopy, *Phys. Rev. E* **72**, 042101 (2005).
- [20] K. D. Kihm, A. Banerjee, C. K. Choi, and T. Takagi, Near-wall hindered Brownian diffusion of nanoparticles examined by three-dimensional ratiometric total internal reflection fluorescence microscopy (3D R-TIRFM), *Exp. Fluids* **37**, 811 (2004).
- [21] B. Lin, J. Yu, and S. A. Rice, Direct measurements of constrained Brownian motion of an isolated sphere between two walls, *Phys. Rev. E* **62**, 3909 (2000).
- [22] W. Russel, E. Hinch, L. Leal, and G. Tieffenbruck, Rods falling near a vertical wall, *J. Fluid Mech.* **83**, 273 (1977).
- [23] M. Lisicki, B. Cichocki, and E. Wajnryb, Near-wall diffusion tensor of an axisymmetric colloidal particle, *J. Chem. Phys.* **145**, 034904 (2016).
- [24] M. De Corato, F. Greco, G. D'Avino, and P. L. Maffettone, Hydrodynamics and Brownian motions of a spheroid near a rigid wall, *J. Chem. Phys.* **142**, 194901 (2015).
- [25] F. C. Cheong and D. G. Grier, Rotational and translational diffusion of copper oxide nanorods measured with holographic video microscopy, *Opt. Express* **18**, 6555 (2010).
- [26] D. F. Katz, J. R. Blake, and S. L. Paveri-Fontana, On the movement of slender bodies near plane boundaries at low Reynolds number, *J. Fluid Mech.* **72**, 529 (1975).
- [27] D. Mukhija and M. J. Solomon, Translational and rotational dynamics of colloidal rods by direct visualization with confocal microscopy, *J. Colloid Interface Sci.* **314**, 98 (2007).
- [28] L. P. Faucheux and A. J. Libchaber, Confined Brownian motion, *Phys. Rev. E* **49**, 5158 (1994).
- [29] R. Hsu and P. Ganatos, The motion of a rigid body in viscous fluid bounded by a plane wall, *J. Fluid. Mech.* **207**, 29 (1989).
- [30] M. De Corato, J. J. M. Slot, H. Uütter, G. D'Avino, P. L. Maffettone, and M. A. Hulsen, Finite element formulation of fluctuating hydrodynamics for fluids filled with rigid particles using boundary fitted meshes, *J. Comput. Phys.* **316**, 632 (2016).
- [31] B. Uma, T. N. Swaminathan, R. Radhakrishnan, D. M. Eckmann, and P. S. Ayyaswamy, Nanoparticle Brownian motion and hydrodynamic interactions in the presence of flow fields, *Phys. Fluids* **23**, 073602 (2011).
- [32] J. T. Padding and W. J. Briels, Translational and rotational friction on a colloidal rod near a wall, *J. Chem. Phys.* **132**, 054511 (2010).
- [33] F. B. Usabiaga, B. Kallemov, B. Delmote, A. P. S. Bhalla, B. E. Griffith, and A. Donev, Hydrodynamic of suspensions of passive and active rigid particles: A rigid multiblob approach, *Commun. Appl. Math. Comput. Sci.* **11**, 217 (2016).
- [34] P. J. Żuk, B. Cichocki, and P. Szymczak, GRPY: An accurate bead method for calculation of hydrodynamic properties of rigid biomacromolecules, *Biophys. J.* **115**, 782 (2018).
- [35] R. Hill and G. Power, Extremum principles for slow viscous flow and the approximate calculation of drag, *Q. J. Mech. Appl. Math.* **9**, 313 (1956).
- [36] S. Kim and S. J. Karrila, in *Microhydrodynamics: Principles and Selected Applications* (Dover Publications, Mineola, New York, 2005), pp. 14–19.
- [37] J. Rotne and S. Prager, Variational treatment of hydrodynamic interaction in polymers, *J. Chem. Phys.* **50**, 4831 (1969).
- [38] E. Wajnryb, K. A. Mizerski, P. J. Żuk, and P. Szymczak, Generalization of the Rotne-Prager-Yamakawa mobility and shear disturbance tensors, *J. Fluid Mech.* **731**, R3 (2013).
- [39] J. R. Blake, A note on the image system for a Stokeslet in a no-slip boundary, *Math. Proc. Camb. Philos. Soc.* **70**, 303 (1971).
- [40] B. Carrasco and J. García de la Torre, Hydrodynamic properties of rigid particles: Comparison of different modeling and computational procedures, *Biophys. J.* **76**, 3044 (1999).
- [41] J. García de la Torre, M. L. Huertas, and B. Carrasco, Calculation of hydrodynamic properties of globular proteins from their atomic-level structure, *Biophys. J.* **78**, 719 (2000).
- [42] S. R. Aragon, Recent advances in macromolecular hydrodynamic modeling, *Methods* **54**, 101 (2011).
- [43] J. Happel and H. Brenner, *Low Reynolds Number Hydrodynamics with Special Applications to Particulate Media* (Martinus Nijhoff Publishers, The Hague, 1983), pp. 42–43.
- [44] S. Kim and S. J. Karrila, *Microhydrodynamics: Principles and Selected Applications* (Dover Publications, Mineola, New York, 2005), pp. 115–117.
- [45] R. Kubo, The fluctuation-dissipation theorem, *Rep. Prog. Phys.* **29**, 255 (1966).
- [46] M. X. Fernandes and J. García de la Torre, Brownian dynamics simulation of rigid particles of arbitrary shape in external fields, *Biophys. J.* **83**, 3039 (2002).
- [47] K. Hinsen, HYDROLIB: A library for the evaluation of hydrodynamic interactions in colloidal suspensions, *Comput. Phys. Commun.* **88**, 327 (1995).
- [48] B. Cichocki and K. Hinsen, Stokes drag on conglomerates of spheres, *Phys. Fluids* **7**, 285 (1995).
- [49] N. Wang, G. A. Huber, and J. A. McCammon, Assessing the two-body diffusion tensor calculated by the bead models, *J. Chem. Phys.* **138**, 204117 (2013).
- [50] R. Kutteh, Rigid body dynamics approach to Stokesian dynamics simulations of nonspherical particles, *J. Chem. Phys.* **132**, 174107 (2010).
- [51] J. W. Swan, J. F. Brady, R. S. Moore, and ChE 174, Modeling hydrodynamic self-propulsion with Stokesian dynamics: Or

- teaching Stokesian dynamics to swim, *Phys. Fluids* **23**, 071901 (2011).
- [52] J. W. Swan and J. F. Brady, Simulation of hydrodynamically interacting particles near a no-slip boundary, *Phys. Fluids* **19**, 113306 (2007).
- [53] S. Delong, F. B. Usabiaga, and A. Donev, Brownian dynamics of confined rigid bodies, *J. Chem. Phys.* **143**, 144107 (2015).
- [54] E. M. Gauger, M. T. Downtown, and H. Stark, Fluid transport at low Reynolds number with magnetically actuated artificial media, *Eur. Phys. J. E* **28**, 231 (2009).
- [55] S. C. Harvey and J. García de la Torre, Coordinate systems for modelling the hydrodynamic resistance and diffusion coefficients of irregularly shaped rigid macromolecules, *Macromolecules* **13**, 960 (1980).
- [56] B. Cichocki, M. L. Ekiel-Jezewska, and E. Wajnryb, Translational Brownian motion for particles of arbitrary shape, *J. Chem. Phys.* **136**, 071102 (2012).
- [57] B. Cichocki, M. L. Ekiel-Jezewska, and E. Wajnryb, Brownian motion of a particle with arbitrary shape, *J. Chem. Phys.* **142**, 214902 (2015).
- [58] J. W. Swan and G. Wang, Rapid calculation of hydrodynamic and transport properties in concentrated solutions of colloidal particles and macromolecules, *Phys. Fluids* **28**, 011902 (2016).
- [59] See Supplemental Material at <http://link.aps.org/supplemental/10.1103/PhysRevE.106.014407> for details regarding the three-, six-, and nine-sphere models of HEWL (Fig. S1, Table S1) and the capsule-like molecule models (Figs. S2 and S3), a full set of results obtained with the scaling approach (Figs. S4–S12), illustrations of the scaling approach performance in re-creating various mobility components (Figs. S13 and S14), and Fig. S15 showing how the time needed to evaluate the mobility tensor matrix scales with the number of subunits in the hydrodynamic model.
- [60] R. Diamond, Real-space refinement of the structure of hen egg-white lysozyme, *J. Mol. Biol.* **82**, 371 (1974).
- [61] E. F. Pettersen, T. D. Goddard, C. C. Huang, G. S. Couch, D. M. Greenblatt, E. C. Meng, and T. E. Ferrin, UCSF Chimera—A visualization system for exploratory research and analysis, *J. Comput. Chem.* **25**, 1605 (2004).
- [62] J. Arvo, Fast random rotation matrices, in *Graphics Gems III (IBM Version)*, edited by D. Kirk (Morgan Kaufmann, San Francisco, 1992), pp. 117–120.
- [63] K. Wüthrich, M. Billeter, and G. Wider, NMR studies of the hydration of biological macromolecules, *Faraday Discuss.* **103**, 245 (1996).
- [64] B. Halle and M. Davidovic, Biomolecular hydration: From water dynamics to hydrodynamics, *Proc. Natl. Acad. Sci. USA* **100**, 12135 (2003).
- [65] L. Zhang, L. Wang, and D. Zhong, Mapping hydration dynamics around a protein surface, *Proc. Natl. Acad. Sci. USA* **104**, 18461 (2007).
- [66] W. S. Price, F. Tsuchiya, and Y. Arata, Lysozyme aggregation and solution properties studied using PDSGE NMR diffusion measurements, *J. Am. Chem. Soc.* **121**, 11503 (1999).
- [67] N. C. Stellwagen, S. Magnusdottir, C. Gelfi, and P. G. Righetti, Measuring the translational diffusion coefficients of small DNA molecules by capillary electrophoresis, *Biopolymers* **58**, 390 (2001).
- [68] M. Długosz and J. M. Antosiewicz, Toward an accurate modeling of hydrodynamic effects on the translational and rotational dynamics of biomolecules in many-body systems, *J. Phys. Chem. B* **119**, 8425 (2015).
- [69] A. Mongruel, N. Lecoq, E. Wajnryb, B. Cichocki, and F. Feuillebois, Motion of a spherocylindrical particle in a viscous fluid in confined geometry, *Eur. J. Mech. B Fluids* **30**, 405 (2011).
- [70] G. Perkins and R. Jones, Hydrodynamic interaction of a spherical particle with a planar boundary: II. Hard wall, *Physica A* **189**, 447 (1992).
- [71] B. Cichocki and R. B. Jones, Image representation of a spherical particle near a hard wall, *Physica A* **258**, 273 (1998).
- [72] S. Kim and S. J. Karrila, *Microhydrodynamics: Principles and Selected Applications* (Dover Publications, Mineola, New York, 2005), pp. 27–31.
- [73] J. Antosiewicz, Computation of the dipole moments of proteins, *Biophys. J.* **69**, 1344 (1995).
- [74] J. Antosiewicz and D. Pörschke, Volume correction for bead model simulations of rotational of rotational friction coefficients of macromolecules, *J. Phys. Chem.* **93**, 5301 (1989).
- [75] J. Antosiewicz and D. Pörschke, Brownian dynamics simulation of electrooptical transients for complex macrodipoles, *J. Phys. Chem.* **97**, 2767 (1993).
- [76] H. M. Berman, J. Westbrook, Z. Feng, G. Gilliland, T. N. Bhat, H. Weissig, I. Shindyalov, and P. E. Bourne, The Protein Data Bank, *Nucl. Acids Res.* **28**, 235 (2000).
- [77] R. Salomon-Ferrer, D. A. Case, and R. C. Walker, An overview of the Amber biomolecular simulation package, *WIREs Comput. Mol. Sci.* **3**, 198 (2013).
- [78] D. A. Case, T. E. Cheatham, III, T. Darden, H. Gohlke, R. Luo, K. Merz, Jr., A. Onufriev, C. Simmerling, B. Wang, and R. Woods, The Amber biomolecular simulation programs, *J. Comput. Chem.* **26**, 1668 (2005).
- [79] D. Brune and S. Kim, Predicting protein diffusion coefficients, *Proc. Natl. Acad. Sci. USA* **90**, 3835 (1993).
- [80] S. Kumar, V. K. Ravi, and R. Swaminathan, Suppression of lysozyme aggregation at alkaline pH by tri-N-acetylchitotriose, *Biochim. Biophys. Acta* **1794**, 913 (2009).
- [81] A. Arkhipov, P. L. Freddolino, and K. Schulten, Stability and dynamics of virus capsids described by coarse-grained modeling, *Structure* **14**, 1767 (2006).
- [82] W. Humphrey, A. Dalke, and K. Schulten, VMD—Visual molecular dynamics, *J. Mol. Graph.* **14**, 33 (1996).